Phase-field simulation of particles rigid body motion at the early stage of sintering in powder bed fusion with electron beam: A proposal for computational efficiency

Finite Elements in Analysis and Design 248 (2025) 104359

Contents lists available at ScienceDirect

Finite Elements in Analysis & Design

journal homepage: www.elsevier.com/locate/finel

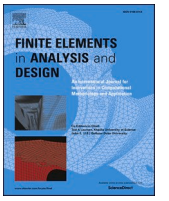

Phase-field simulation of particles rigid body motion at the early stage of sintering in powder bed fusion with electron beam: A proposal for computational efficiency

Manuela Galati [a], Giovanni Rizza [a,*]

[a] Department of Management and Production Engineering (DIGEP), Integrated Additive Manufacturing Center (IAM@Polito), Politecnico di Torino, Corso Duca degli Abruzzi 24, 10129, Torino, Italy

ARTICLE INFO

Keywords:
Electron beam melting
Ti6Al4V
Sintering
Additive manufacturing
Powder
Phase field

ABSTRACT

The sintering of powder particles prior to full melting is a defining feature of the powder bed fusion with electron beam (PBF-EB) process, distinguishing it from other metal additive manufacturing techniques. Sintering involves the movement of atoms toward contact points between adjacent particles, leading to neck formation and growth. This atomic movement is driven by the high working temperatures of PBF-EB, which activate diffusion mechanisms and induce rigid body motion (RBM) of particles. While research on the numerical analysis of diffusion is growing, the motion of the particles occurring during the PBF-EB and its relevance are still unexplored. This work uses a phase field model to capture the physics of early-stage sintering in PBF-EB, incorporating both diffusion and RBM driven by vacancy migration. The influence of RBM parameters on neck formation and growth during the sintering of Ti6Al4V particles under PBF-EB conditions is investigated. Simulations encompass different process phases and durations (from seconds to hours), including the preheating of the layer and the cooling of the build. In addition, this work addresses the computational challenges of modelling RBM and proposes a novel approach to enhancing diffusion coefficients to emulate RBM effects, significantly reducing simulation times. Results indicate that incorporating RBM accelerates sintering and leads to larger neck formation compared to diffusion alone, although computational time increases by 30 %. Consequently, RBM should be prioritised in scenarios where its impact is critical, such as the preheating phase of PBF-EB. In contrast, during the process, the neck growth can be analysed by the novel proposed approach which significantly enhances computational efficiency while effectively capturing the influence of RBM on neck growth.

1. Introduction

Powder bed fusion with electron beam (PBF-EB) is an additive manufacturing (AM) process for producing metallic components. The process has been developed for industrial applications which are mainly focused on aerospace [1,2] and medical sectors [3]. Applications in these sectors are possible because the high temperatures and the vacuum during the process limit residual stress, cracking and material contamination. The use of an electron beam is the key aspect of the process. Thanks to the use of electromagnetic lenses, the beam can rapidly vary its diameter and the beam scanning velocity, dynamically adjusting the amount of heat supplied

* Corresponding author.
E-mail address: giovanni.rizza@polito.it (G. Rizza).

https://doi.org/10.1016/j.finel.2025.104359
Received 25 January 2025; Received in revised form 12 April 2025; Accepted 12 April 2025
Available online 21 April 2025

during the process [4]. This allows the energy to be focused in a small area reaching the melting temperature or achieving a distributed heating of the powder bed defocusing the beam [5]. Therefore, the electron beam is used not only to selectively melt the metallic powder bed according to the desired shape but also to keep a constant temperature during the process using distributed heat [6]. This task is accomplished by the so-called pre-heating phase, which aims to reach and keep the powder bed at a temperature approximately equal to 60–70 % of the melting point of the processed material [7]. Therefore, the process phases are the following and repeated in sequence up to the build completion.

a) Pre-heating of the powder. During pre-heating the defocused electron beam scans the whole powder layer with high speed (approximately 15000 mms^{-1}) and beam current (approximately 30 mA) [6].
b) Selectively melting the powder according to the cross-section determined after the slicing phase.
c) Lowering the build table and powder raking.

When the build is completed, it cools inside the build chamber until 350 K. After production, the components are enclosed in an agglomerate of sintered powder, which is then disaggregated, sieved, collected, and reused. The formation of this powder agglomerate is due to the high temperature during the process, which activates the sintering. As a consequence, a bridge of solid material, identified as the neck, is formed at the contact point among the powder particles. The neck is shaped as a one-sheet hyperboloid forming a smooth bridge among the powder particles. The dimension of the restricted section of the neck is called neck radius and is usually adopted as a characteristic parameter to describe the neck growth and the sintering evolution.

The sintering occurring during the PBF-EB process is similar to the traditional pressure-less solid-state sintering, where the necking occurs only because of the time and temperature [8]. However, contrary to the manufacturing processes based on sintering, owing to the particle size and heating rate, the sintering during a PBF-EB is extremely faster. The primary goal of sintering in PBF-EB is to form a sufficient neck between adjacent particles to facilitate heat and electrical transfer within the powder bed and toward the solid substrate, ensuring a stable powder bed temperature. Therefore, sintering during PBF-EB is intentionally limited to an early stage, as the neck must not be too large. An excessive heat transfer could lead to a localised overheating or overcooling, compromising the thermal stability of the process, which is crucial for material processing. Therefore, the densification mechanism through sintering is not desired in PBF-EB, as it would affect the process dynamics and material properties. A neck from 5 μm to 10 μm is usually formed within the first 5 s after the deposition of the powder during the preheating, which is the key phase for the thermal stability of the process [7].

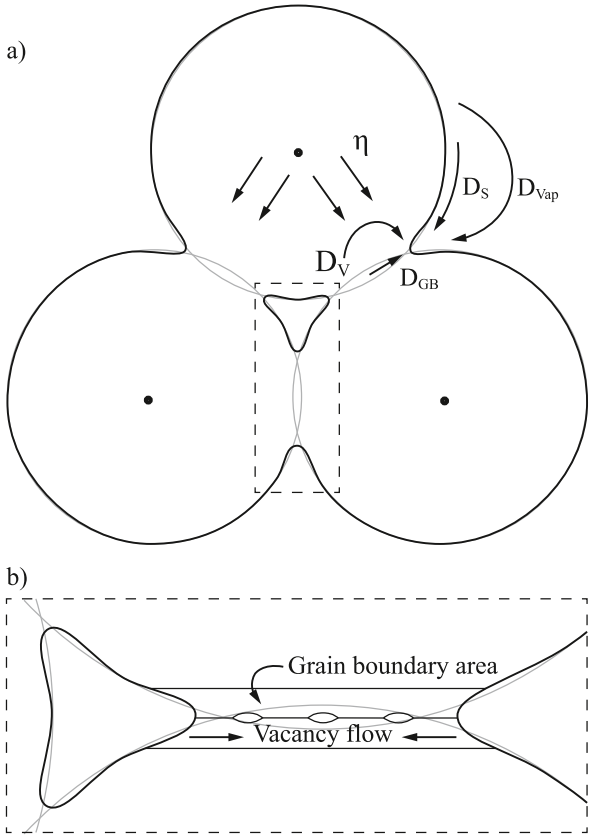

Fig. 1. Movements of atoms during sintering. The tail of the arrow indicates the source, while the tip indicates the sink. a) shows the different diffusion mechanisms and the viscous flow. b) shows the mechanism of vacancy annihilation via the grain boundary of the particles.

The neck growth continues at a lower rate of approximately 1×10^{-3} μm/s until the temperature inside the build chamber is higher than the sintering temperature, which for Ti6Al4V is approximately 800 K [7]. This time varies according to the height of the build but generally is shorter than 30 min [7], with a final maximum neck radius in the order of 15 μm–20 μm, about one fifth of the typical particle size [7].

Practically, the sintering consists of a movement of atoms due to several diffusion mechanisms, showed in Fig. 1 (surface (D_s), volume (D_v), grain boundary (D_{GB}) and vapour (D_{vap}) diffusions) and viscous flow (η) [8]. Fig. 1 a) shows graphically the direction of atom diffusion, with the arrows showing the source and sink for each mechanism. The sintering mechanisms can be distinguished according to their densifying or non-densifying nature [9]. Surface (D_s) or vapour diffusion (D_{vap}) are classified as non-densifying mechanisms since these contribute to particle reshaping and neck growth [8]. Under the effect of these non-densifying mechanisms, atoms move from the surface of the powder particles toward the contact area among the particles. The other mechanisms (volume (D_v) and grain boundary (D_{GB}) diffusion and viscous flow (η)), instead, contribute to both neck growth and densification. The densification occurs because of the annihilation of porosities (or vacancies) among the different powder particles via the grain boundary. These porosities are generated at the surface of the neck and move along the grain boundary toward the centre of the neck, driven by the reduction of the chemical energy, as shown in Fig. 1 b). These porosities are filled by atoms which move in the opposite direction to the vacancies flux, leading to a movement of the material toward the contact point of the particles. The annihilation of porosity finally results in a rigid body motion (RBM) of the particles toward the centre of mass of the system. The RBM, together with the neck growth, controls the densification of the powder structure.

Although manufacturing processes based on sintering usually aim to achieve high densification [10] at the end of the process, the sintering in PBF-EB, as mentioned above, aims and is limited to neck formation [7]. The process of sintering is then controlled to have a neck large enough to give stability to the powder bed, preventing the smoke phenomenon [11] and providing the proper thermal [12] and electrical conductivity [11], which allows the proper heat and electric charges transfer. On the other hand, the neck size must be limited to ensure that no heat accumulations are created in the powder bed and the sintered cake disintegrates easily without significant particle shape modification, facilitating recycling [13]. This balance is obtained using experimental tests, in which the operator evaluates the sintering degree qualitatively and the temperature evolution with the aim of properly calibrating the preheating parameters. However, owing to the process conditions, the temperature evolution is only measured at the bottom of the start plate, and therefore, the relationship between the pre-heating parameters and the sintering degree may be biased by the heat transfer along the build direction and permanence time of the powder at a high temperature. The focus of preheating and neck formation is driven by thermal conductivity in the powder bed directly influencing melt pool formation, stability, and the cooling rate of the material. These factors, in turn, determine the microstructure development and, ultimately, the mechanical properties of the processed material. Online monitoring of the neck growth and powder properties may provide insight into the sintering for better tuning of the process, but such microscale observation at the heating rate of the process is today unfeasible [14]. Numerical simulations currently remain a reliable alternative to gaining a deeper knowledge of neck evolution [15] and more in general for predicting, calibrating and optimising the PBF-EB process [16]. For example, Rizza et al. [12] showed a numerical framework where neck evolution data serve as input for an analytical model to estimate the thermal conductivity of the powder bed in PBF-EB. In general, Yi et al. [17] showed that various numerical methodologies can be used to analyse the sintering at different length scales. However, the most adopted approaches are based on the discrete element method [18], Monte Carlo [19], Phase Field (PF) [17] and macroscopic continuum models [20]. Discrete element methods have high computational costs, limiting the analysis to a nanometric scale for microseconds. Monte Carlo is stochastic and relies on simplified assumptions that make it difficult to describe real phenomena, like diffusion. The macroscopic continuum model does not consider the actual particle structure of the system and relies on averaged parameters that may oversimplify the sintering process. PF is considered one of the most appropriate modelling techniques for sintering simulation [21] because it accounts for morphology changes or particle agglomeration [7].

PF modelling approaches the sintering as the system evolves to reduce its free energy. This energy is modelled as a function of conserved and non-conserved variables. Conserved variables describe the density of the system, while non-conserved are used to identify the particles. The time evolution of these quantities is described by the Cahn-Hilliard equation for conserved variables and the Allen-Cahn for the non-conserved ones [22]. The RBM of the particles is modelled using specific terms that rely on numerical parameters that bind the physical phenomenon of vacancy annihilation to the actual rigid translation of the powder particles. The literature on including the RBM in the simulation verifies only the correctness of the numerical modelling, neglecting, for simplicity, the characteristics of the process or the material [9,23,24]. The challenging task is the proper simulation of the rigid translation and rotation of the particles [25] and the computational resources required for the calculation with respect a only diffusion sintering simulation [26].

For PBF-EB, RBM is, in most cases, neglected in the studies based on PF numerical modelling [7,27]. Therefore, the effect on the sintering degree of the modelling parameters used to describe the RBM of the particles remains unrevealed and meaningless for the analysis of the sintering in the PBF-EB process. The time scale for the sintering in PBF-EB is much shorter (from a few seconds to a couple of hours) than manufacturing processes based on sintering for densification, such as the pressure-less solid-state sintering or powder metallurgy sintering (dozens of hours). Therefore, owing to the rapid neck growth, the absence of densification, and the limited neck size, it remains unclear whether the contribution of RBM to neck formation in the early stages of sintering during the PBF-EB justifies the computational resources required to account for this mechanism.

An alternative approach could be considered to overcome the challenges associated with selecting RBM parameters. If the RBM effect is relatively limited, the increase in neck size caused by RBM could be emulated by using higher diffusion coefficients, thereby avoiding the direct implementation of RBM for the particles. This idea was inspired by a statement in the introduction of Seiz's work [28], though Seiz himself neither proposed nor implemented such an approach or demonstrated its effectiveness.

This study preliminarily investigates the influence of RBM parameters on the evolution of neck radius and the positioning of powder particles during sintering under PBF-EB conditions. By systematically varying RBM parameters in a numerical design of experiments, optimal values suitable for the PBF-EB process are identified. To enhance simulation efficiency, the study further explores the potential to simplify the model by replacing the explicit modelling of particle RBM with pseudo diffusion coefficients. These coefficients are calibrated to replicate the neck evolution under PBF-EB conditions when the RBM is considered.

2. Materials and methods

2.1. Numerical modelling

A PF model was adopted in this work to analyse the sintering during PBF-EB. As mentioned in the introduction, in PF, the evolution of a system made of particles is described by the conserved (c) and non-conserved (η) variables. The conserved variable brings information about the density or molar fraction, providing information about the local composition [24]. The value of the conserved variable is set to 1 inside the solid material and 0 outside. The non-conserved variable provides details about the local structure and particle orientation, allowing the distinction among the different powder particles [24]. Non-conserved variables are set equal to 1 inside the ith particle and 0 elsewhere. The evolution of conserved and non-conserved variables in time and space is driven by the reduction of the free energy of the system, described by equation (1) [24].

$$F = \int \left[f(c, \eta_i) + \frac{1}{2} k_c |\nabla c|^2 + \frac{1}{2} \sum k_{\eta_i} |\nabla \eta_i|^2 \right] dV \tag{1}$$

The first term of the free energy represents the non-equilibrium bulk free energy, while the second and third terms correspond to the energy contribution from surface and grain boundaries, respectively. The bulk free energy can be approximated as a Landau-type potential as described by equation (2)

$$f(c, \eta_i) = Ac^2(1 - c)^2 + B\left[c^2 + 6(1 - c)\sum_i \eta_i{}^2 - 4(2 - c)\sum_i \eta_i{}^3 + 3\left(\sum_i \eta_i{}^2 \right)^2 \right] \tag{2}$$

where A and B are two constants, described in equations (3) and (4), respectively.

$$A = \frac{12\gamma_S - 7\gamma_{GB_{ij}}}{\delta} \tag{3}$$

$$B = \frac{\gamma_{GB_{ij}}}{\delta} \tag{4}$$

where γ_s and γ_{GBij} are the surface and grain boundary energy, respectively, and δ is the interface width, i.e. the distance over which the transition of the field variables occurs.

The gradient coefficients k_c and $k_{\eta i}$ of equation (1) can be evaluated according to equations (5) and (6), respectively.

$$k_c = \frac{3}{4}\delta\left(2\gamma_s - \gamma_{GB_{ij}} \right) \tag{5}$$

$$k_{\eta_{ij}} = \frac{3}{4}\left(\delta\gamma_{GB_{ij}} \right) \tag{6}$$

The free energy of equation (1) evolves because the conserved (c) and non-conserved (η_i) variables evolve. The evolution in time of the conserved variable (c) is described by the Cahn-Hilliard equation [29,30] and includes the RBM of the particles according to the modelling proposed by Chockalingam et al. [31] (equation (7)):

$$\frac{\partial c(\mathbf{x}, t)}{\partial t} = \nabla \cdot \left[\mathbf{M} \nabla \frac{\partial F}{\partial c(\mathbf{x}, t)} - c\sum_t \mathbf{v}_{adv_i} \right] \tag{7}$$

The term **M** represents the concentration mobility tensor, described in equation (8)

$$\mathbf{M} = \frac{\mathbf{D}\Omega}{k_b T} \tag{8}$$

where **D** is the diffusivity tensor, described by equation (9), Ω is the molar volume of the considered material, k_b is the Boltzmann constant and T is the absolute temperature of the system.

$$\mathbf{D} = \mathbf{D}_V + \mathbf{D}_S + \mathbf{D}_{GB} \tag{9}$$

The diffusivity tensor **D**, given as the sum of the volume ($\mathbf{D}_v$), surface ($\mathbf{D}_s$), and grain boundary ($\mathbf{D}_{GB}$) diffusion vectors, can be calculated using equations (10)–(12) [31].

$$\mathbf{D}_V = D_V \phi_b(c)\mathbf{I} \tag{10}$$

$$\mathbf{D}_S = D_S \phi_S(c)\mathbf{T}_S \tag{11}$$

$$\mathbf{D}_{GB} = D_{GB} \sum_i \sum_j \eta_i \eta_j \mathbf{T}_{GB_{ij}} \tag{12}$$

where D_V, D_S and D_{GB} represent the volume, surface and grain boundary diffusion coefficients, respectively. $\phi_b(c)$ and $\phi_S(c)$ represent the interpolation functions and $\mathbf{I}$, $\mathbf{T}_S$ and $\mathbf{T}_{GBij}$ represent the identity matrix and the projection tensor for surface and grain boundary, respectively [31].

The diffusion coefficients D_V, D_S and D_{GB} can be modelled using an Arrhenius-type equation, reported in equation (13)

$$D = D^0 \exp\left(\frac{Q}{k_B T}\right) \tag{13}$$

where D^0 is a pre-exponential factor characterising the diffusion mechanism, Q is the activation energy specific for the diffusion mechanism, k_B is the Boltzmann constant, and T is the absolute temperature of the system.

The interpolation functions $\phi_b(c)$ and $\phi_S(c)$ can be calculated as in equations (14) and (15).

$$\phi_b(c) = c^3\left(10 - 15c + 6c^2\right) \tag{14}$$

$$\phi_S(c) = 30c^2(1-c)^2 \tag{15}$$

The projection tensors $\mathbf{T}_S$ and $\mathbf{T}_{GBij}$ are described by equations (16) and (17), respectively.

$$\mathbf{T}_S = \mathbf{I} - \mathbf{n}_S \otimes \mathbf{n}_S \tag{16}$$

$$\mathbf{T}_{GB_{ij}} = \mathbf{I} - \mathbf{n}_{GB_{ij}} \otimes \mathbf{n}_{GB_{ij}} \tag{17}$$

where, $\mathbf{n}_S$ and $\mathbf{n}_{GB}$ denote the vector normal to the interface particle-void and the grain boundary, respectively.

The evolution in time of the non-conserved variables η_{ij} is described by the Allen-Cahn equation (equation (18)), modified to keep in account for the presence of the rigid body motion [31].

$$\frac{\partial \eta_i(\mathbf{x},t)}{\partial t} = L\frac{\partial F}{\partial \eta_i(\mathbf{x},t)} - \nabla \cdot \eta_i \mathbf{v}_{adv_i} \tag{18}$$

Where L represents the order parameter scalar mobility, described by equation (19)

$$L = \frac{\vartheta_{GB}\gamma_{GB}}{k_{\eta_{ij}}} \tag{19}$$

where ϑ_{GB} is the grain boundary mobility and is a material dependent parameter.

The terms $c\sum_t \mathbf{v}_{adv_i}$ and $\nabla \cdot \eta_i \mathbf{v}_{adv_i}$ in equation (7) and equation (18), respectively, accounts for the mobility of the particles. These terms are function of the advection velocity $\left(\mathbf{v}_{adv_i}\right)$ of the ith particle toward the other particles. This is described by equation (20)

$$\mathbf{v}_{adv_i}(\mathbf{x},t) = \mathbf{v}_{t_i}(\mathbf{x},t) + \mathbf{v}_{r_i}(\mathbf{x},t) \tag{20}$$

where $\mathbf{v}_{adv_i}(\mathbf{x},t)$ is the sum of the translation of the particles $\mathbf{v}_{t_i}(\mathbf{x},t)$ and the rotation of the particles $\mathbf{v}_{r_i}(\mathbf{x},t)$. These velocities are a function of time (t) and space (x) and are related to the ith particle. These are defined by equations (21) and (22).

$$\mathbf{v}_{t_i}(\mathbf{x},t) = \frac{m_t}{V_i}\mathbf{F}_i \tag{21}$$

$$\mathbf{v}_{r_i}(\mathbf{x},t) = \frac{m_r}{V_i}\mathbf{T}_i \times \left[\mathbf{x} - \mathbf{x}_{c_i}\right] \tag{22}$$

where, m_t and m_r are the RBM coefficients referred to the translation and rotation mobility, respectively. These parameters describe how effectively the powder particles undergo a translation and a rotation as a consequence of the force and torque acting on the particles. The effect of the force and torque is reduced by the volume of the particles V_i with larger particles subject to the same force or torque undergoing a smaller rotation or translation. $\mathbf{x}_{c_i}$ represents the position of the centre of mass of the particle and is evaluated by equation (23)

$$\mathbf{x}_{c_i} = \frac{1}{V_i}\int_V \mathbf{x}\eta_i d^3x \tag{23}$$

$\mathbf{F}_i$ and $\mathbf{T}_i$ of equations (21) and (22) are the force and the torque acting on the ith particle, calculated according to equations (24) and (25).

$$\mathbf{F}_i = \int_V d\mathbf{F}_i \tag{24}$$

$$\mathbf{T}_i = \int_V \left[\mathbf{x}\text{-}\mathbf{x}_{c_i}\right] \times d\mathbf{F}_i \tag{25}$$

where $\mathbf{F}_i$ represents the force density between the particles. In this work, the calculation of $d\mathbf{F}_i$ is performed using the formulation proposed by Wang [24], equation (26)

$$d\mathbf{F}_i = k\sum_{j\neq i}(c - c_o)\langle\eta_i\eta_j\rangle\left[\nabla\eta_i - \nabla\eta_j\right]d^3x \tag{26}$$

where k is a RBM constant referred to the stiffness and c_0 represents the equilibrium concentration. The product $\langle\eta_i\eta_j\rangle$ is defined in equation (27)

$$\langle\eta_i\eta_j\rangle = \begin{cases} 1 \text{ for } \eta_i\eta_j \geq \eta_{ij}^{min} \\ 0 \text{ for } \eta_i\eta_j < \eta_{ij}^{min} \end{cases} \tag{27}$$

Where η_{ij}^{min} is a RBM constant referred to a threshold concentration value that defines the particle grain boundary interface trough η_i and η_j.

2.2. Design of numerical experiment

The free energy (equation (1)), the Cahn-Hilliard (equation (7)) and the Allen-Cahn (equation (18)) equations of the PF model were solved using the finite element method (FEM). The simulations were implemented in the Multiphysics Object Oriented Simulation Environment (MOOSE), an open-source FEM simulation environment developed at Idaho National Lab [32]. The domain was bidimensional and included three particles with a diameter equal to 80 μm (Fig. 2), representing the average particle distribution size generally used in the PBF-EB process [16]. The three powder particles (Part. 1, Part. 2 and Part. 3 in Fig. 2) of diameter (D, in Fig. 2 a)) equal to 80 μm are in contact with each other at two points (Fig. 2 a)). The centres of the particles were positioned at the vertices of an equilateral triangle with sides measuring 80 μm. This configuration of the powder particles includes a closed porosity between them, representative of a typical formation in the powder bed [33–35]. After raking, the powder bed consists of powder particles stacked one on top of the other, forming the actual layer thickness. It is important to note that the actual layer thickness in powder bed fusion AM is always greater than the preset layer thickness used during the slicing phase, to account for the natural porosities in the powder bed that disappear during the melting phase [35]. During sintering, at the contact points, the neck is formed and grows with time and temperature. At the end of the sintering, an example of the final domain shape is illustrated in Fig. 2 b), with a neck formed at the contact point with a certain neck radius (x in Fig. 2 b)). The neck radius is measured as the smallest distance between the segment that connects the centre of the powder particles and the vertex of the hyperbola, which approximates the bridge of material between two powder

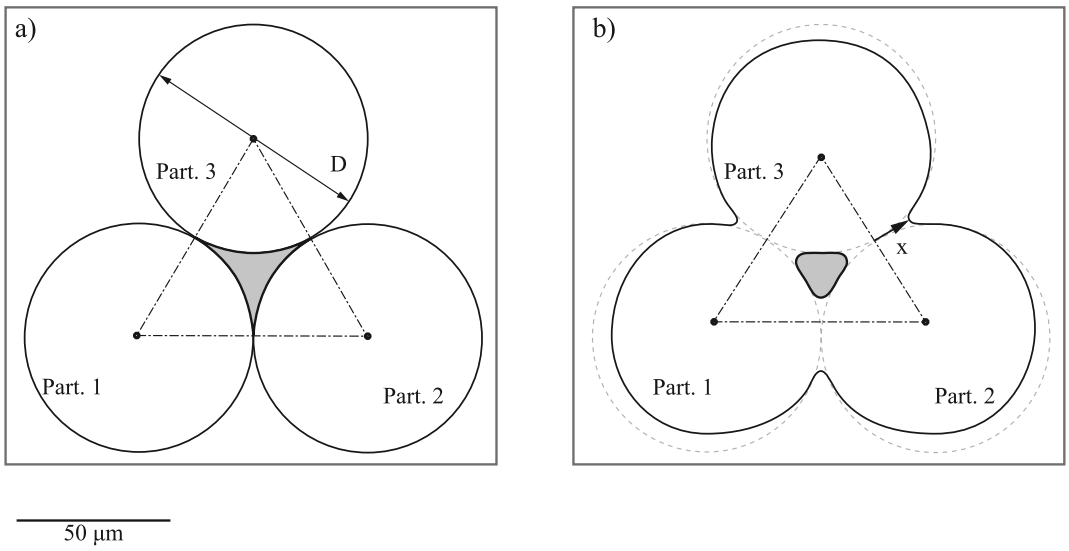

Fig. 2. Configuration of the powder particles in the simulation domain. The porosity among the powder particles is highlighted as a light grey area. a) configuration before sintering and b) configuration after sintering occurred. D represents the particle diameter, and x represents the neck radius.

particles. This configuration of the powder particles produces a pore at the centre of the simulation domain. This pore can be initially approximated with a triangle with three cusps at the contact point of the powder particles (the area shaded in grey in Fig. 2 a)). The evolution of the system during sintering leads to a smoothening of the edges, with a pore at the centre of the system that progressively becomes more round (as shown in Fig. 2 b)).

Fig. 3 shows the simulation domain and the mesh adopted for the simulations. The simulation domain had a dimension of 170 μm × 160 μm (Fig. 3) and was meshed using QUAD9 elements with a dimension of 1 μm (Fig. 3). The simulation domain was set to be large enough to ensure that a distance of at least 5 μm is present between the edges of the domain and the powder particles. The refinement of the mesh was tuned so that in stable simulation conditions, the interface of the particles was approximated by a minimum of four elements, according to Qin and Bhadeshia [22].

For all simulations, the material of the particles was Ti6Al4V. Table 1 reports the material parameters for the diffusion mechanisms ϑ_{GB} (equation (19)), γ_{GB} and γ_s (equation (3)) Q_s, D_s^0, Q_v and D_v^0 (equation (13)). The value of these constants was retrieved from the literature (References in Table 1). The molar mass Ω was calculated according to the nominal composition of Ti6Al4V and it is reported in Table 1. For the current work, the grain boundary diffusion (D_{GB}) was considered equal to one-tenth of the surface diffusion (D_S), according to Ref. [31]. Vapour diffusion was neglected due to the lack of numerical values available in the literature and due to the fact that this is usually three orders of magnitude smaller than surface diffusion [24].

Following the findings of Shi et al. [9], which showed that rigid-body rotation has little to no impact on the sintering rate, the present study does not account for the rigid rotation of the particles. To exclude the rotation of the particles, the coefficient m_r in equation (22) was considered equal to zero.

The output parameters of the simulation that measure the sintering progression were the neck radius and the translation of the centre of the powder particles. According to Seiz [28], the neck radius, x (Fig. 2) was calculated as $x = \frac{\int 4\,\eta_i\eta_j dV}{2\delta}$ where δ is the interface width, which for the current work was set equal to 2 μm. The calculation was automatically done using a postprocessor coded for the scope. The position of the centre of the powder particles was evaluated using the GrainTracker postprocessor [38] available in the phase field module of MOOSE. The neck radius and the centre position were calculated at each simulation step. Information on the centre of the powder particles was adopted to calculate the position of the centre of mass of the system.

The magnitude of the translation of the centre of the powder particles was obtained by calculating the translation distance with respect to the initial position. The equilibrium concentration c_0 (equation (26)) was set to 0.982. Therefore, the remaining parameters for describing the RBM were m_t, η_{ij}^{min} and k. The effect of the RBM was investigated using several simulations, grouped as follows:

- "Set A" which investigated the influence of RBM parameters on a second time scale with temperature growth which simulates the pre-heating phase alone (Fig. 4 - segment AB).
- "Set B" which considered an hour time scale with a temperature increase and decrease that simulates the pre-heating of a layer (Fig. 4 - segment AB), the heating (Fig. 4 - segment B'C) and cooling of a build during a PBF-EB process (Fig. 4 - CD).
- "Set C" was conducted under the same conditions as "Set B″, but the modelling of RBM was excluded. The advection terms in Cahn-Hilliard (equation (7)) and Allen-Cahn (equation (18)) equations were neglected by setting m_t equal to zero in equation (21) and their effect on the neck growth is emulated by adjusted diffusion coefficients.

The temperature load is presented in equation (28) [25], where T is the temperature of the powder bed, expressed in K, and t is the simulation time, expressed in seconds. Fig. 4 graphically represents the temperature load described in equation (28). The pre-heating

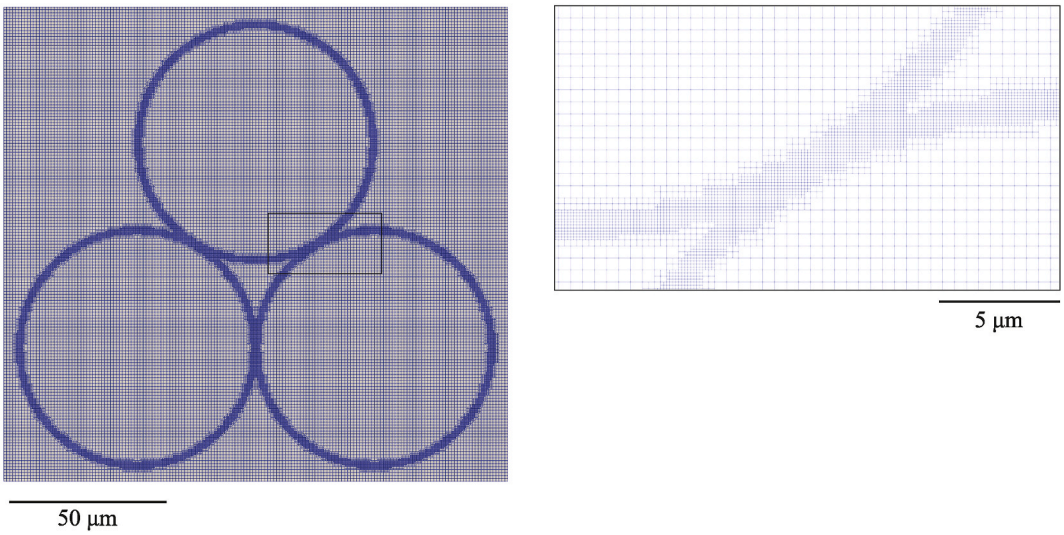

Fig. 3. Mesh adopted for the simulation with detail on how the mesh is refined at the boundary area.

Table 1
Material properties for PF sintering simulation of Ti6Al4V.

Property	Value	Units of measurement	Reference
ϑ_{GB}	10^{-11}	$m^{-4}J^{-1}s^{-1}$	[27]
γ_{GB}	0.81	Jm^{-2}	[36]
γ_S	2.1	Jm^{-2}	[36]
Q_s	1.19×10^{-19}	J	[27]
D_S^0	9.33×10^{-8}	m^2s^{-1}	[27]
Q_v	3.2×10^{-19}	J	[37]
D_V^0	2.92×10^{-19}	m^2s^{-1}	[37]
Ω	4.051×10^{-29}	m^3	

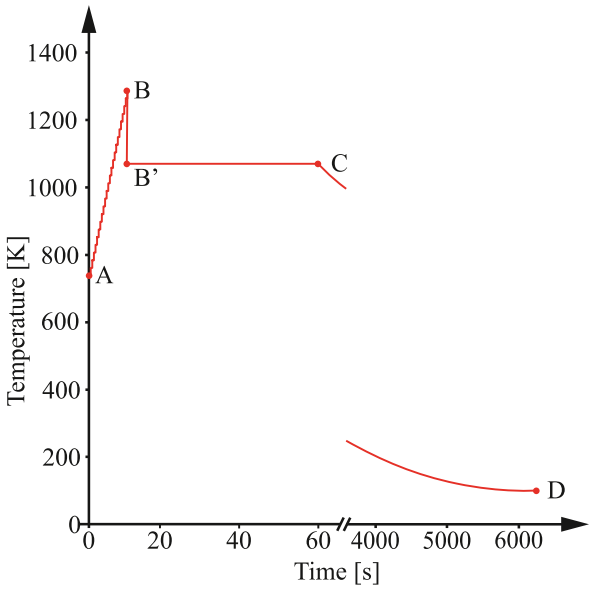

Fig. 4. Graphic representation of the temperature load for the simulations of Set A (segment AB) and sets B and C (complete temperature profile AD).

phase is simulated by increasing the temperature from 845 K to 1273 K over 9.5 s (segment AB in Fig. 4). In line with the modelling assumptions in Ref. [7], the temperature is raised in 25 steps, simulating a series of beam passages [7,39], with an incremental increase of approximately 17 K per passage. Between each passage, the temperature is held constant. This effect is achieved using the function *"int"*, which rounds the result of the ratio t/0.38 to the nearest whole number. The constant 0.38 is derived from dividing the pre-heating duration (9.5 s) by 25 steps. Following pre-heating, the melting phase begins, where the beam is rapidly focused onto a small area corresponding to the beam's cross-section. Since the neck is already formed and contributes to heat transfer, the heat is applied locally, causing the temperature in the powder bed, far from the melt pool as the case considered in this work, to drop slightly. This temperature drop is rapid until it stabilises at 1131 K. The melting phase lasts 60 s (segment B'C in Fig. 4). After the melting phase, a new layer of cold powder is spread over the previous one, which slowly cools down following a parabolic profile (Fig. 4 - CD), as described by equation (28), reaching 353 K, the temperature at which the build could be extracted. This cooling profile is estimated based on thermocouple measurements below the start plate [40]. The build extraction temperature is reached after 6240 s (1 h and 44 min).

All the simulations were performed on a desktop computer with an Intel i5 processor (up to 3.58 GHz) and 32 Gb of RAM memory.

$$T(t) = \begin{cases} 845 + \text{int}\left(\dfrac{t}{0.38}\right) \cdot 17.12 & 0 \le t \le 9.5 \\ 1131 & 9.5 < t \le 60 \\ 2.75 \cdot 10^{-5}(t\text{-}60)^2\text{-}0.27(t\text{-}60) + 1131 & t > 60 \end{cases} \tag{28}$$

2.2.1. *Analysis of m_t, η_{ij}^{min} and k on a seconds-scale timescale (only heating)*

Set A investigated the effect of varying m_t, η_{ij}^{min} and k on the neck radius and the particle centre position. In the design of the numerical experiment, each factor was tested at three different levels: m_t was set to 100, 150 and 200; η_{ij}^{min} to 0.1, 0.125 and 0.15; k to 0.01, 0.05 and 0.1. The order of magnitude of the selected numerical values was set according to the experimental tuning performed in

Ref. [25].

A total of 27 numerical simulations were performed under temperature and time conditions characteristic of the preheating of the Ti6Al4V powder performed at each layer of the PBF-EB process before the melting [25] (Segment AB in Figure Fig. 4, Equation (28)). The initial time step for the simulations was set equal to 0.01 s, while the maximum time step was set to 0.05 s to accurately describe the neck growth.

For the sake of comparison, the results of simulations conducted for the design of the numerical experiment were compared to a simulation conducted considering the same duration (9.5 s) and the same temperature evolution (Equation (28)) but excluding the RBM of the powder particles.

To facilitate comparison among the different cases of set A, the neck radius and the position of the powder particle centre were analysed at the end of the preheating step, after 9.5 s. The statistical analyses to evaluate the effect of the RBM parameters were conducted using the software Minitab 17.

2.2.2. Analysis of m_t, η_{ij}^{min} and k on an hours-scale timescale (heating and cooling)

Set B examined the effect of RBM under a more realistic temperature history for the powder bed, incorporating temperature variations caused by heat transfer during pre-heating, melting, and the subsequent cooling as the process progressed (Fig. 4, Equation (28)). The initial time step was set to 0.01 s, while the maximum step size was limited to 70 s to capture correctly the neck growth.

The RBM parameters were set equal to $m_t = 100$, $\eta_{ij}^{min} = 0.1$ and $k = 0.01$. Larger values of m_t, η_{ij}^{min} and k generate non-physical deformation due to a non-realistic translation that continues even when the system has reached the equilibrium (temperature below the sintering start).

In addition, for the sake of comparison, the same simulation (duration and temperature) was performed, neglecting the RBM of the particles.

2.2.3. Adjustment of the diffusion coefficients to emulate the neck growth under heating and cooling on an hours-scale timescale

As mentioned above, this work wants to address the challenges associated with determining the RBM coefficient and the computational expense of explicitly modelling RBM by tuning the diffusion coefficients. Theoretically, particle movement facilitates neck growth, suggesting that modifications to the diffusion coefficients should aim to accelerate diffusion mechanisms when the modelling of the particle movement is excluded. In this study, to explore the effectiveness of this approach, the pre-exponential factors of the diffusion mechanisms (D_S^0 and D_V^0 in equation (13)) were increased with respect to the properties reported in Table 1. The values of D_S^0 and D_V^0 were assumed to increase from the previously tested value proportionally by 1.5 % at each simulation. During the simulation, the neck radius growth was iteratively compared to the counterpart obtained in the simulation with the RBM of Set B till obtaining a closer match among the curves.

Table 2 summarises the value of the pseudo diffusion coefficients adopted for the simulations of Set C. All these simulations considered the same duration of the process (1 h and 44 min) and temperature profile (equation (28)) considered in simulations of Set B.

3. Results and discussion

3.1. Analysis of mt, η_{ij}^{min} and k on a seconds-scale timescale (only heating)

The simulations of Set A required, on average, 9 h and 40 min each, while the simulation that neglected the RBM required less than 7 h. In agreement with the literature, the neck radius grows with the temperature and the neck radii are the same among the three couples of particles since the particles have identical diameters [7]. Therefore, the results are reported only considering a couple of particles. For that couple of particles, the neck size was measured at each simulation step. Accordingly, for each numerical simulation of Set A, 198 measurements were extracted, resulting in a total of 5346 measurements. To avoid overcrowding the graphical representation of these measurements, all values are represented within a ribbon in Fig. 5. The dashed curve in Fig. 5 represents the neck radius evolution for the simulation that neglected the RBM of the particles and it is included for reference. As it can be observed, the neck radius obtained considering the RBM is always larger. This shows that RBM accelerates sintering, independently of the values of m_t, η_{ij}^{min} and k considered.

Table 2
Values of the pseudo diffusion coefficients adopted for the simulations of Set C.

	D_S^0 [m^2s^{-1}]	D_V^0 [m^2s^{-1}]
Case 0	9.33×10^{-8}	2.92×10^{-19}
Case 1	9.47×10^{-8}	2.96×10^{-19}
Case 2	9.61×10^{-8}	3.01×10^{-19}
Case 3	9.75×10^{-8}	3.05×10^{-19}
Case 4	9.90×10^{-8}	3.10×10^{-19}
Case 5	1.01×10^{-7}	3.14×10^{-19}
Case 6	1.02×10^{-7}	3.19×10^{-19}

A comparison is possible with the results of Shi et al. [9] and Seiz [28]. These studies considered a sintering evolution in terms of the area of the void comprised among the particles and the length of the powder particle chain, respectively, which is different from the neck radius considered in this work. Despite this difference, the results of Shi et al. [9] and Seiz [28] demonstrate that including RBM produces a smaller void area and shorter particle chains. This means that including RBM produces faster sintering, which agrees with the results obtained in the current work.

At the last simulation step, corresponding to 9.5 s, the neck sizes for each simulation of Set A are reported in Table 3, while the neck radius excluding the RBM is 7.34 μm. The largest neck radius was obtained for $m_t = 200$, $\eta_{ij}^{min} = 0.1$ and $k = 0.1$ with a neck of 7.82 μm, which is about 6.5 % larger than the case that did not consider the RBM of the particles.

Fig. 6 shows the main effect plot based on the data reported in Table 3. It can be noticed that all the RBM parameters affect the mean neck radius, but k has the strongest effect. η_{ij}^{min} has the opposite effect with respect to m_t and k: higher values of η_{ij}^{min} hide the neck growth.

From the main effect plot and the data reported in Table 3, itis visible that larger values of m_t and k and smaller values of η_{ij}^{min} produce larger values of neck radius. This is because larger values of k produce larger values of the forces that push the particles one against the other (equation (26)). While larger values of m_t directly produce larger values of the translation velocities (equation (21)). These effects produce an enhanced material flow and a faster interface evolution. The first effect is due to the modification of the local free energy density gradient (first term of equation (7)) in the Chan-Hilliard equation (equation (7)). The second effect is due to an increased advection term contribution (the second term of equation (18)) in the Allen-Cahn equation (equation (18)). Both these effects result in larger neck radius values.

On the contrary, smaller values of η_{ij}^{min} produce larger neck radii (equation (27)) since η_{ij}^{min} is a threshold value that discriminates the value of the product $\langle \eta_i \eta_j \rangle$. Considering smaller values of η_{ij}^{min} means considering a larger interface among the powder particles and, consequently, a larger value of the force among the particles (equation (26)) since this depends on the amplitude of the grain boundary among the particles. Then, considering smaller values of η_{ij}^{min} results in a larger value of the neck radius.

The trends obtained from these simulations align with the trends identified in the literature for η_{ij}^{min} and k [25]. Regarding m_t, the trend identified in this work is in contrast with, e.g. Ref. [25]. However, the tested values in this work were orders of magnitude different with respect to the ones reported in Ref. [25]. In fact, the three values tested in Ref. [25] spanned the broad numerical range from 1 to 1000, which may hide a local behaviour of the neck growth. Selecting a narrower range means that higher values of m_t produce faster neck growth, which agrees with Shi et al. [9].

As mentioned in the introduction, the neck growth due to the movement of the particles is also highlighted by the movement of the centres of the particles. Table A1 in Appendix 1 reports the magnitude of the rigid translation of the powder particles at the last step of the simulation after 9.5 s. The translation of particles 1 and 2 is the same for each simulation, while the magnitude of the translation of particle 3 is, on average, 12 % smaller.

The magnitude of the rigid translation depends on the set of RBM parameters considered. The largest translation of the centre of the particles was found in the case of $m_t = 200$, $\eta_{ij}^{min} = 0.125$ and $k = 0.1$ with a rigid translation of 0.42 μm for particles 1 and 2 and 0.31 μm for particle 3. Fig. 7 shows the magnitude and the direction of the rigid translation of the particles in the case of $m_t = 200$, $\eta_{ij}^{min} = 0.125$ and $k = 0.1$. The reason behind the different magnitudes of translation may be the asymmetric distance of the powder particles from the simulation domain. As reported in section 2.2, a square simulation domain allowed to maintain a distance of at least 5 μm between the powder particles and the edges of the simulation domain. Moreover, this simulation domain does not hinder the evolution of the neck among the particles, as would do a simulation domain that is simply an offset of the three powder particles considered. This,

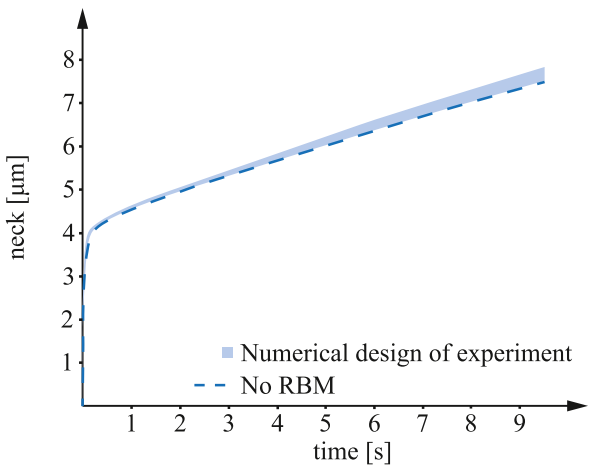

Fig. 5. Ribbon Plot for the neck radius evolution for all the simulations of the design of numerical experiment. The dashed curve represents the neck evolution without RBM.

Table 3
Values of neck radius obtained at the end of the simulation for the simulations of Set A.

Neck size [μm]	$m_t = 100$			$m_t = 150$			$m_t = 200$		
$\eta_{ij}^{min} \downarrow$ k →	0.01	0.05	0.1	0.01	0.05	0.1	0.01	0.05	0.1
0.1	7.52	7.58	7.66	7.53	7.62	7.74	7.54	7.66	7.82
0.125	7.52	7.56	7.62	7.52	7.59	7.68	7.53	7.62	7.74
0.15	7.51	7.54	7.58	7.52	7.56	7.62	7.52	7.58	7.66

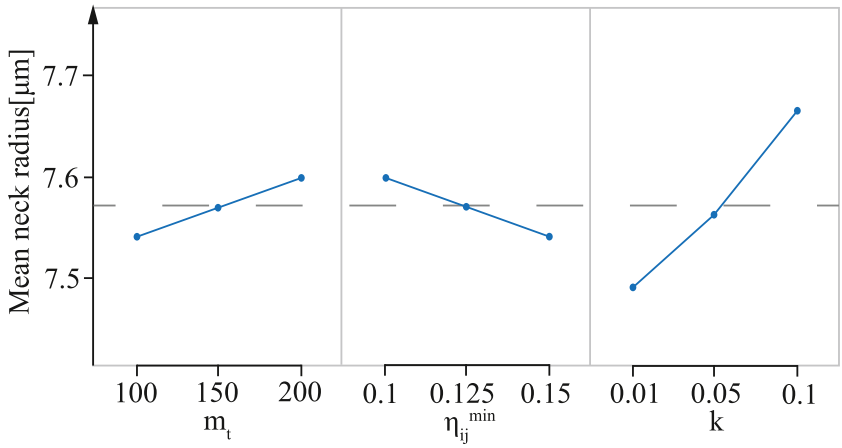

Fig. 6. Main effect plot for the results obtained from the simulations of the design of numerical experiment.

however, comes with the drawback of an asymmetry in the distance of the particles with respect to the edges of the simulation domain. Considering the horizontal distance at the centre of the particle, particles 1 and 2 have a smaller distance from the edges than particle 3. Such a large horizontal distance for particle 3 allows for a smoothening of the concentration gradient, with a smaller edge effect on particle 3 than on particles 1 and 2. This results in an unbalanced force system, with particle 3 experiencing a force that is smaller than the force acting on particles 1 and 2. This unbalanced force system also results in a vertical translation of the centre of mass of the system toward particle 3 of approximately 0.05 μm.

The influence of RBM on neck radius growth ratio and rigid translation is also visible in the evolution of the area of the void

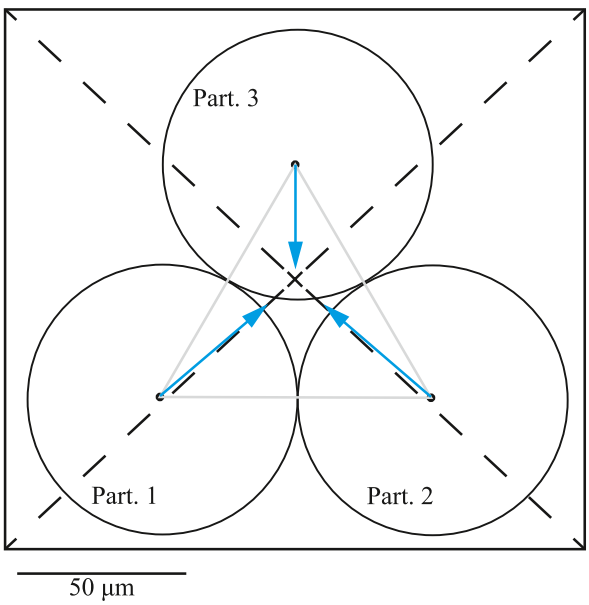

Fig. 7. Rigid translation of the centre of the powder particles due to RBM. The blue arrows show the direction of the movement and the magnitude, amplified of 100 times. The case represented is the one in which $m_t = 200$, $\eta_{ij}^{min} = 0.125$ and $k = 0.1$.

comprised among the particles (Fig. 2). When no RBM is included, after 9.5 s, the void area reduces by approximately 6 % compared to the initial shape. This area reduction is due to only the growth of the neck among the powder particles. When the RBM of the particles is included, the shrinkage of the area is more significant and equal to approximately 10 % compared to the initial shape.

3.2. Analysis of m_t, η_{ij}^{min} and k on a hours-scale timescale (heating and cooling)

As for the simulations of Set A, also for the simulations of Set B, the neck radius considered for the analyses was the one among particles 1 and 2. At the end of the sintering simulation, after 1 h and 44 min (6240 s), the neck radius obtained for the simulation without RBM was 13.04 μm, while for the simulation that considered the RBM (considering $m_t = 100$, $\eta_{ij}^{min} = 0.1$ and $k = 0.01$) of the particles, the neck radius was 13.19 μm. Including the RBM in the sintering simulation produces a final neck radius that is 1.1 % larger. While the magnitude of the neck radius is larger for the simulations that include melting and cooling, the difference between simulations that consider RBM and those that neglect RBM at the end of the simulations is smaller than the analogous simulation of Set A (considering the same RBM parameters).

Including the RBM of the particles produces a displacement of 1.1 μm for particles 1 and 2, and a displacement of 0.99 μm for particle 3. The direction of the displacement was the same as Set A and is shown in Fig. 7, while the magnitude of the displacement is larger than that obtained for the same simulations of Set A, meaning that the particle movement also continues after the temperature increase and during the cooling. Surprisingly, a comparison between the displacement measured in Set A and Set B reveals that nearly 50 % of particle movement occurs within a few seconds during the temperature ramp-up (preheating) phase, while the remaining displacement takes place over several hours as the process continues.

The effect of RBM is also visible on the void area comprised between the powder particles (Fig. 2). At the end of the simulations that do not consider the RBM of particles, this area is 304 μm^2, while in the case of the simulation that considers the RBM of the particles is 279 μm^2, which approximately 9 % smaller than the area measured in absence of RBM. This result agrees with the work of Shi et al. [9], in which including the RBM of the particles in the simulation accelerates the shrinkage of the void area comprised among the particles.

As visible from the result of the simulation of Set A, the use of a different combination of RBM parameters, such as $m_t = 200$, $\eta_{ij}^{min} = 0.15$ and $k = 0.1$ may produce a larger effect on the neck radius and particle positions, also for simulations that consider the melting and the cooling. However, such kind of parameters produced unrealistic effects of deformation of the domain due to the action of advection force (Equation (26)) even when the system is below the sintering start temperature of approximately 800 K for Ti6Al4V [7]. Fig. 8 shows the domain which includes three particles with $m_t = 200$, $\eta_{ij}^{min} = 0.15$ and $k = 0.1$ at 4632 s of sintering, the instant at which the simulation stopped. For temperatures below 800 K, the redistribution of material due to diffusion is not occurring, so the deformation of the system should also follow. Instead, this does not happen because the advection force is only a function of the conserved and non-conserved variables, not directly governed by the temperature of the system (Equation (26)). For this reason, the advection force keeps acting on the powder particles producing a plastic deformation, as if an external force pushes the particles together. This results in the notches visible at the interface of the particles in Fig. 8 that are not representative of a physical condition, where the diffusion phenomena would have allowed the redistribution of the material and the smoothening of the neck. This also affects the porosity at the centre of the system, which presents sharp edges that are not representative of the physical behaviour of the system.

Considering the time required to perform the simulation, the simulation without RBM of the particles required 6 h and 12 min, while the simulation that considered RBM required 6 h and 42 min.

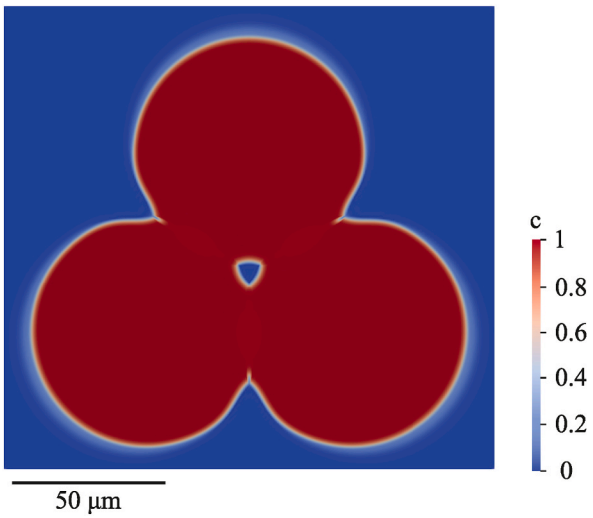

Fig. 8. Unphysical deformations occurring for a simulation of Set B conducted with $m_t = 200$, $\eta_{ij}^{min} = 0.15$ and $k = 0.1$ at 4632 s.

3.3. Adjustment of the diffusion coefficients to emulate the neck growth under heating and cooling on an hours-scale timescale

As described in the methodology section, Set C consisted of six simulations in which the neck radius was measured at each simulation till reaching convergence with the results of Set B. This result was achieved in Case 6 by using D_S^0 equal to 1.02×10^{-7} Jm^{-2} and D_V^0 equal to 3.19×10^{-19} Jm^{-2}. Fig. 9 a) shows the neck radius evolution in the case of purposely increased diffusion coefficients and the curve obtained in Set B considering the RBM of the particles. Fig. 9 b) and c) represent the concentration field at the last step of the simulation, for the case of simulation that considers the RBM of the particles (Fig. 9 b)) and the simulation that considers the pseudo diffusion coefficients (Fig. 9 c)). As visible in Fig. 9 a), the two curves referred to simulation with RBM and pseudo diffusion coefficients overlap. There is a slight difference in the initial 1000 s of sintering, with values of neck radius slightly larger in the case of simulation with purposely amplified diffusion coefficients of Set C. As an example, at 500 s, the neck radius for the simulation with increased diffusion coefficients was 12.70 μm, while the neck for the simulation that considered the RBM of the particles was 12.63 μm. This difference can be considered within the numerical error. The analogies among the two cases are also visible by comparing the concentration field reported in Fig. 9 b) and c).

The amplification of the diffusion coefficients led to a reduction of the computing time equal to 7.5 % compared to the analogous simulation carried considering the RBM of the particles. Evidently, this method leaves out the tracking of the movement of the centre of the powder particles, which may be useful to track the shrinkage of the volume. However, limited to the sintering at an early stage that occurs in the PBF-EB condition, it appears that this shrinkage could be neglected (the distance between the centre of the particle and the centre of the domain is 2 % smaller when considering the RBM of the particles) because the process is not aimed at the material densification but only to the neck formation which is the parameter for controlling key properties of the powder such as the thermal conductivity [12].

4. Conclusions

In the context of the sintering at an early stage that occur in the PBF-EB process, this work investigates the effect of including the RBM of the particles when simulating sintering with a PF model and shows the potential to simplify the model by replacing the explicit modelling of particle RBM with purposely amplified diffusion coefficients.

This study reveals that within the explored range of values for the rigid body motion parameters for the Ti6Al4V during PBF-EB, the rigid body motion of particles during pre-heating in the PBF-EB process has a limited impact on the neck radius and rigid translation of the particles, in which, at the maximum, the neck radius was found to be approximately 6.5 % larger than the case without RBM. On the other hand, the computing time increased by 30 %. The difference becomes more negligible when the neck evolution is observed on hours time scale simulations, which include a cooling phase of the powder bed. The computing time is 7.5 % larger compared to a simulation which excludes the RBM, but the neck radius at the end of the process was only 1.1 % larger than the case without RBM, which may be considered within the numerical error. This is mainly due to a rigid translation limited to approximately 1 μm. Particularly, almost 50 % of this translation occurs in the first seconds of the process during the ramp-up of the temperature, while the remaining 50 % takes place over several hours in the remaining 99 % of the process time. This limited effect could be explained by the fact that the temperature after the pre-heating phase and the melting phase (less than 70 s in total) is decreasing. This observation also confirms the absence of densification or powder porosity shrinkage in the powder bed of PBF-EB due to the limited effect of the RBM. However, for the hour-long simulations, it was not possible to investigate all the RBM parameter combinations considered in the simulation of sintering during preheating. The reason is that some RBM parameter combinations led to nonphysical deformations of

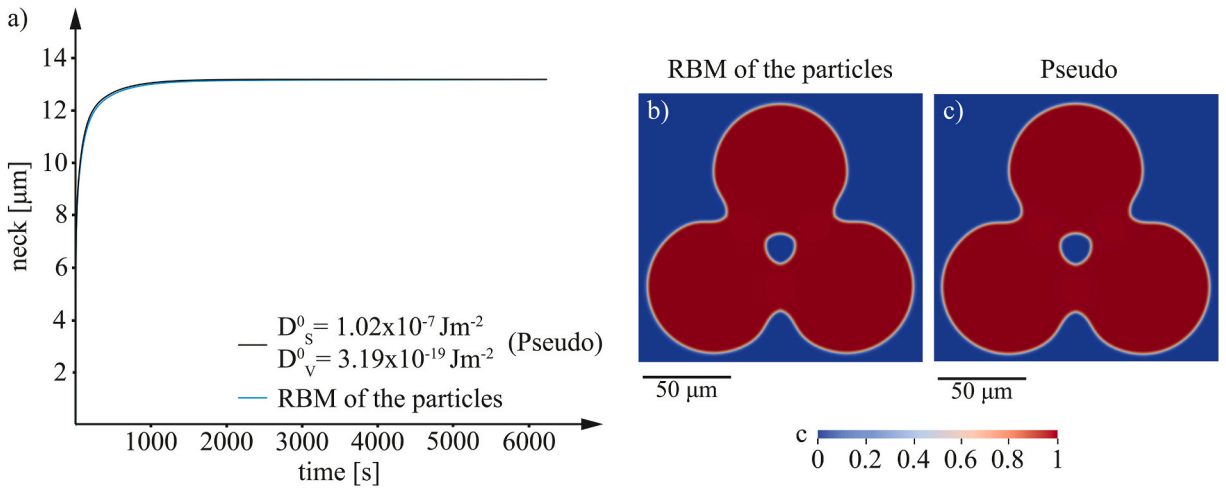

Fig. 9. a) Comparison of the neck evolution in the case of purposely increased D_0^S and D_0^V to that obtained when considering the RBM of the particles. Concentration field at the end of the simulation, considering b) the RBM of the particles and c) the pseudo diffusion coefficients.

the system due to the presence of the RBM when the system is below the sintering start temperature. To solve this issue and consider more combinations of RBM parameters future works are needed to modify the PF equations accordingly.

In light of these findings, it appears that the RBM should be carefully considered only when its effect is preponderant. This corresponds to the first step of the PBF-EB process, the preheating phase. On the other hand, due to the absent or negligible densification, at this step, the neck size is of paramount importance for determining key properties of the powder bed, such as thermal conductivity [12]. In view of that, the knowledge of the neck radius is the parameter to be preferred. In this regard, the proposed approach to replace the explicit modelling of the RBM of the particles by amplifying the effect of the diffusion mechanism RBM demonstrated to be valuable to contain the computational efforts without sacrificing the accuracy of the neck size prediction. With this approach, the computational time was reduced by 30 %, with no substantial differences in the neck growth. This preliminary work provides a foundation for further investigation, particularly in determining whether increasing pseudo-diffusion coefficients depends on simulation parameters such as particle size, powder distribution and temperature profile and whether a predictive model can be developed to calibrate them automatically, eliminating the need for manual calibration.

CRediT authorship contribution statement

Manuela Galati: Writing – review & editing, Visualization, Supervision, Methodology, Investigation, Conceptualization. **Giovanni Rizza:** Writing – review & editing, Writing – original draft, Visualization, Software, Methodology, Investigation, Formal analysis, Data curation.

Funding

This research did not receive any specific grant from funding agencies in the public, commercial, or not-for-profit sectors.

Declaration of competing interest

The authors declare that they have no known competing financial interests or personal relationships that could have appeared to influence the work reported in this paper.

Appendix A

Table A1
Magnitude of the rigid translation for each particle of the system for different values of RBM parameters.

Case($m_t_\eta_{ij}^{min}$_k)	Particle 1 [μm]	Particle 2 [μm]	Particle 3 [μm]
100_0.1_0.01	0.26	0.26	0.29
100_0.1_0.05	0.29	0.29	0.24
100_0.1_0.1	0.38	0.38	0.27
100_0.125_0.01	0.25	0.25	0.30
100_0.125_0.05	0.27	0.27	0.25
100_0.125_0.1	0.34	0.34	0.24
100_0.15_0.01	0.25	0.25	0.29
100_0.15_0.05	0.24	0.24	0.28
100_0.15_0.1	0.30	0.30	0.24
150_0.1_0.01	0.26	0.26	0.29
150_0.1_0.05	0.33	0.33	0.25
150_0.1_0.1	0.42	0.42	0.30
150_0.125_0.01	0.25	0.25	0.27
150_0.125_0.05	0.30	0.30	0.24
150_0.125_0.1	0.40	0.40	0.28
150_0.15_0.01	0.25	0.25	0.30
150_0.15_0.05	0.26	0.26	0.25
150_0.15_0.1	0.34	0.34	0.26
200_0.1_0.01	0.25	0.25	0.28
200_0.1_0.05	0.38	0.38	0.27
200_0.1_0.1	0.47	0.47	0.39
200_0.125_0.01	0.26	0.26	0.29
200_0.125_0.05	0.34	0.34	0.24
200_0.125_0.1	0.42	0.42	0.31
200_0.15_0.01	0.25	0.25	0.27
200_0.15_0.05	0.30	0.30	0.24
200_0.15_0.1	0.39	0.39	0.29

Appendix B

To verify the absence of three-grain and evaluate the suitability of the phase-field formulation for simulating early-stage sintering, the scalar field T_η was computed across the simulation domain. This field was used to quantify the local overlap of three distinct grain order parameters and provides a means to identify potential triple-phase regions. The threshold set to identify potential overlapping is set equal to 0.01, which corresponds roughly to a third-phase contribution of 0.0025 in an ideal grain boundary. Equation (B.1) defines the field T_η, where η_1, η_2 and η_3 refer to the non-conserved variable for each particle considered.

$$T_\eta = 27\eta_1\eta_2\eta_3 \tag{B1}$$

The analysis performed on the simulations included in the manuscript showed that T_η remains several orders of magnitude below the threshold throughout the domain, including at the neck and pore regions. Therefore, the computed values of T_η indicate that these gradients do not result in substantial three-phase overlap. This confirms that the formation of triple-phase junctions is effectively absent in the current simulations. Therefore, the adopted phase-field framework can be considered appropriate for capturing the physics of early-stage sintering in PBF-EB under the investigated conditions.

As an example, Fig. B1 shows the scalar field T_η calculated for the simulation of Set B that considered the RBM of particles, with a white contour line marking the grain boundary region.

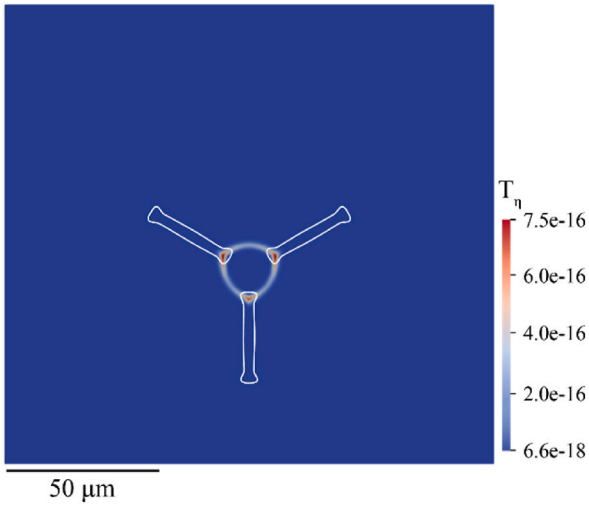

Fig. B1. Scalar field T_η calculated for the simulation of set B that includes RBM of the particles. The white line marks the grain boundary region.

Data availability

Data will be made available on request.

References

[1] S. Knippscheer, G. Frommeyer, Intermetallic TiAl(Cr,Mo,Si) alloys for lightweight engine parts, Adv. Eng. Mater. 1 (1999) 187–191, https://doi.org/10.1002/(SICI)1527-2648(199912)1:3/4<187::AID-ADEM187>3.0.CO;2-F.
[2] H. Clemens, H. Kestler, Processing and applications of intermetallic γ-TiAl-based alloys, Adv. Eng. Mater. 2 (2000) 551–570, https://doi.org/10.1002/1527-2648(200009)2:9<551::AID-ADEM551>3.0.CO;2-U.
[3] F. Calignano, M. Galati, L. Iuliano, P. Minetola, Design of additively manufactured structures for biomedical applications: a review of the additive manufacturing processes applied to the biomedical sector, J. Healthc. Eng. 2019 (2019) 9748212, https://doi.org/10.1155/2019/9748212.
[4] C. Körner, E. Attar, P. Heinl, Mesoscopic simulation of selective beam melting processes, J. Mater. Process. Technol. 211 (2011) 978–987, https://doi.org/10.1016/j.jmatprotec.2010.12.016.
[5] J. Milberg, M. Sigl, Electron beam sintering of metal powder, Prod. Eng. Res. Dev. 2 (2008) 117–122, https://doi.org/10.1007/s11740-008-0088-2.
[6] S.M. Gaytan, L.E. Murr, F. Medina, E. Martinez, M.I. Lopez, R.B. Wicker, Advanced metal powder based manufacturing of complex components by electron beam melting, Mater. Technol. 24 (2009) 180–190, https://doi.org/10.1179/106678509X12475882446133.
[7] G. Rizza, M. Galati, L. Iuliano, A phase-field study of neck growth in electron beam powder bed fusion (EB-PBF) process of Ti6Al4V powders under different processing conditions, Int. J. Adv. Manuf. Technol. 123 (2022) 855–873, https://doi.org/10.1007/s00170-022-10204-4.
[8] H.E. Exner, E. Arzt, Sinter. Process. (1983), https://doi.org/10.22028/D291-23791.
[9] R. Shi, M. Wood, T.W. Heo, B.C. Wood, J. Ye, Towards understanding particle rigid-body motion during solid-state sintering, J. Eur. Ceram. Soc. 41 (2021) 211–231, https://doi.org/10.1016/j.jeurceramsoc.2021.09.039.
[10] Z.Z. Fang, Sintering of Advanced Materials, Elsevier, 2010.
[11] J. Ye, J. Renner, C. Körner, Z. Fu, Electron-optical observation of smoke evolution during electron beam powder bed fusion, Addit. Manuf. 70 (2023) 103578, https://doi.org/10.1016/j.addma.2023.103578.

[12] G. Rizza, M. Galati, Powder bed fusion with electron beam: the interplay of sintering, porosity, and coordination number in modelling the powder thermal conductivity through a novel tortuosity formulation, Int. J. Heat Mass Tran. 234 (2024) 126055, https://doi.org/10.1016/j.ijheatmasstransfer.2024.126055.
[13] Z. Lin, S. Dadbakhsh, A. Rashid, Developing processing windows for powder pre-heating in electron beam melting, J. Manuf. Process. 83 (2022) 180–191, https://doi.org/10.1016/j.jmapro.2022.08.063.
[14] H.-H. König, N. Semjatov, G. Spartacus, P. Bidola, C. Ioannidou, J. Ye, J. Renner, U. Lienert, G.A. Faria, B. Wahlmann, M. Wildheim, U. Ackelid, F. Beckmann, P. Staron, P. Hedström, C. Körner, G. Lindwall, MiniMelt: an instrument for real-time tracking of electron beam additive manufacturing using synchrotron x-ray techniques, Rev. Sci. Instrum. 94 (2023) 125103, https://doi.org/10.1063/5.0177255.
[15] T. Kraft, H. Riedel, Numerical simulation of solid state sintering; model and application, J. Eur. Ceram. Soc. 24 (2004) 345–361, https://doi.org/10.1016/S0955-2219(03)00222-X.
[16] M. Galati, Chapter 8 - electron beam melting process: a general overview, in: J. Pou, A. Riveiro, J.P. Davim (Eds.), Additive Manufacturing, Elsevier, 2021, pp. 277–301, https://doi.org/10.1016/B978-0-12-818411-0.00014-8.
[17] M. Yi, W. Wang, M. Xue, Q. Gong, B.-X. Xu, Modeling and simulation of sintering process across scales, Arch. Comput. Methods Eng. 30 (2023) 3325–3358, https://doi.org/10.1007/s11831-023-09905-0.
[18] A.A. Mahmood, M. Elektorowicz, A review of discrete element method research on particulate systems, IOP Conf. Ser. Mater. Sci. Eng. 136 (2016) 012034, https://doi.org/10.1088/1757-899X/136/1/012034.
[19] M.P. Anderson, D.J. Srolovitz, G.S. Grest, P.S. Sahni, Computer simulation of grain growth—I. Kinetics, Acta Metall. 32 (1984) 783–791, https://doi.org/10.1016/0001-6160(84)90151-2.
[20] H. Palmour, T.M. Hare, Rate controlled sintering revisited, in: G.C. Kuczynski, D.P. Uskoković, H. Palmour, M.M. Ristić (Eds.), Sintering'85, Springer US, Boston, MA, 1987, pp. 17–34, https://doi.org/10.1007/978-1-4613-2851-3_2.
[21] S. Biswas, D. Schwen, J. Singh, V. Tomar, A study of the evolution of microstructure and consolidation kinetics during sintering using a phase field modeling based approach, Extreme Mech. Lett. 7 (2016) 78–89, https://doi.org/10.1016/j.eml.2016.02.017.
[22] R.S. Qin, H.K. Bhadeshia, Phase field method, Mater. Sci. Technol. 26 (2010) 803–811, https://doi.org/10.1179/174328409X453190.
[23] S. Biswas, D. Schwen, V. Tomar, Implementation of a phase field model for simulating evolution of two powder particles representing microstructural changes during sintering, J. Mater. Sci. 53 (2018) 5799–5825, https://doi.org/10.1007/s10853-017-1846-3.
[24] Y.U. Wang, Computer modeling and simulation of solid-state sintering: a phase field approach, Acta Mater. 54 (2006) 953–961, https://doi.org/10.1016/j.actamat.2005.10.032.
[25] G. Rizza, M. Galati, P. Antonioni, L. Iuliano, Effect of the sintering conditions on the neck growth during the powder bed fusion with electron beam (PBF-EB) process, J. Manuf. Mater. Process 7 (2023) 55, https://doi.org/10.3390/jmmp7020055.
[26] A. Nakazawa, S. Sakane, T. Takaki, Multi-phase-field modeling and high-performance computation for predicting material microstructure evolution during sintering, J. Mater. Res. Technol. 34 (2025) 1803–1816, https://doi.org/10.1016/j.jmrt.2024.12.171.
[27] W. Yan, W. Ma, Y. Shen, Powder sintering mechanisms during the pre-heating procedure of electron beam additive manufacturing, Mater. Today Commun. 25 (2020) 101579, https://doi.org/10.1016/j.mtcomm.2020.101579.
[28] M. Seiz, Effect of rigid body motion in phase-field models of solid-state sintering, Comput. Mater. Sci. 215 (2022) 111756, https://doi.org/10.1016/j.commatsci.2022.111756.
[29] J.W. Cahn, J.E. Hilliard, Free energy of a nonuniform system. I. Interfacial free energy, J. Chem. Phys. 28 (1958) 258–267, https://doi.org/10.1063/1.1744102.
[30] J.W. Cahn, On spinodal decomposition, Acta Metall. 9 (1961) 795–801, https://doi.org/10.1016/0001-6160(61)90182-1.
[31] K. Chockalingam, V.G. Kouznetsova, O. van der Sluis, M.G.D. Geers, 2D Phase field modeling of sintering of silver nanoparticles, Comput. Methods Appl. Mech. Eng. 312 (2016) 492–508, https://doi.org/10.1016/j.cma.2016.07.002.
[32] G. Giudicelli, A. Lindsay, L. Harbour, C. Icenhour, M. Li, J.E. Hansel, P. German, P. Behne, O. Marin, R.H. Stogner, J.M. Miller, D. Schwen, Y. Wang, L. Munday, S. Schunert, B.W. Spencer, D. Yushu, A. Recuero, Z.M. Prince, M. Nezdyur, T. Hu, Y. Miao, Y.S. Jung, C. Matthews, A. Novak, B. Langley, T. Truster, N. Nobre, B. Alger, D. Andrs, F. Kong, R. Carlsen, A.E. Slaughter, J.W. Peterson, D. Gaston, C. Permann, 3.0 - MOOSE: enabling massively parallel multiphysics simulations, SoftwareX 26 (2024) 101690, https://doi.org/10.1016/j.softx.2024.101690.
[33] S. Grigoriev, R. Ableyeva, A. Korotkov, R. Khmyrov, T. Tarasova, A. Gusarov, Powder bed surface relief formation and denudation in selective laser melting, Int. J. Adv. Manuf. Technol. 123 (2022) 543–558, https://doi.org/10.1007/s00170-022-10197-0.
[34] S.R. Jaggannagari, W.H. Kan, L.N.S. Chiu, G. Proust, A. Huang, Y. Gan, R.K. Annabattula, Numerical and experimental analysis of powder bed homogeneity through multi-layer spreading in additive manufacturing, Addit. Manuf. 97 (2025) 104571, https://doi.org/10.1016/j.addma.2024.104571.
[35] H. Chen, Q. Wei, Y. Zhang, F. Chen, Y. Shi, W. Yan, Powder-spreading mechanisms in powder-bed-based additive manufacturing: experiments and computational modeling, Acta Mater. 179 (2019) 158–171, https://doi.org/10.1016/j.actamat.2019.08.030.
[36] T.A. Roth, P. Suppayak, The surface and grain boundary free energies of pure titanium and the titanium alloy Ti6Al4V, Mater. Sci. Eng. 35 (1978) 187–196, https://doi.org/10.1016/0025-5416(78)90120-9.
[37] S. Nemat-Nasser, W.G. Guo, J.Y. Cheng, Mechanical properties and deformation mechanisms of a commercially pure titanium, Acta Mater. 47 (1999) 3705–3720, https://doi.org/10.1016/S1359-6454(99)00203-7.
[38] GrainTracker | MOOSE, (n.d.). https://mooseframework.inl.gov/source/postprocessors/GrainTracker.html (accessed March 21, 2025).
[39] J. Böhm, C. Breuning, M. Markl, C. Körner, A new approach of preheating and powder sintering in electron beam powder bed fusion, Int. J. Adv. Manuf. Technol. 133 (2024) 3769–3784, https://doi.org/10.1007/s00170-024-13966-1.
[40] D. Cannizzaro, P. Antonioni, F. Ponzio, M. Galati, E. Patti, S. Di Cataldo, Machine learning-enabled real-time anomaly detection for electron beam powder bed fusion additive manufacturing, J. Intell. Manuf. 36 (2025) 2105–2119, https://doi.org/10.1007/s10845-024-02359-6.